Electrochimica Acta 134 (2014) 35–48

Contents lists available at ScienceDirect

Electrochimica Acta

journal homepage: www.elsevier.com/locate/electacta

Role of CO_2 in Methanol and Water Transport in Direct Methanol Fuel Cells

Seunghun Jung*, Yongjun Leng[1], Chao-Yang Wang[2]

Electrochemical Engine Center, Department of Mechanical and Nuclear Engineering, The Pennsylvania State University, University Park, PA 16802, USA

ARTICLE INFO

Article history:
Received 28 December 2013
Received in revised form 14 April 2014
Accepted 15 April 2014
Available online 26 April 2014

Keywords:
direct methanol fuel cell
DMFC
CO_2
carbon dioxide
modeling

ABSTRACT

CO_2 gas produced in a DMFC during methanol oxidation reaction is typically removed out of the cell through the anode channel while liquid fuel mixture is supplied from the anode channel to the anode porous media. This induces a two-phase flow, which makes it difficult to understand mass transport phenomena in a DMFC. This paper discusses the effect of CO_2 on two-phase flow and mass transport phenomena in a DMFC with a multi-dimensional model. The role of CO_2 in controlling water and methanol transport in DMFCs is theoretically investigated. Multi-D DMFC model explains that amount of CO_2 in the anode controls not only water transport by capillary diffusion, but also methanol transport by both molecular diffusion and capillary diffusion. Two DMFCs (conventional cell and CO_2 breathing cell) are fabricated and tested to confirm the theoretical result acquired from the simulation.

1. Introduction

During electrochemical reaction in a DMFC, water is produced in the cathode from oxygen reduction reaction (ORR) and CO_2 is produced in the anode from methanol oxidation reaction (MOR) as byproducts. In order to maintain steady cell operation, produced CO_2 should be removed out of the cell. Produced CO_2 in the anode catalyst layer is basically in gas phase and typically removed through the anode channel out of the cell. During this CO_2 removal process, it is known that CO_2 gas brings on a strong two-phase flow in the anode channel as shown in Fig. 1(a), which causes a large pressure drop along the anode channel and makes study of DMFC difficult. In addition, typically at high current density operation, CO_2 gas forms slugs which may block the interface between the anode channel and the anode porous media, which prevent the liquid fuel from spreading well into the anode porous media. For the above reason, it is important to consider CO_2 removal for channel design. For example, typical DMFC hardly uses parallel channels on the anode side, although parallel channels have advantages of less pressure drop or even species distribution than serpentine channels. The reason is possible CO_2 slugs that block some anode flow channels and may cause dead regions in the cell.

There are several experimental studies conducted about CO_2 in DMFC. Most of them focus on CO_2 flow behavior in the anode channel [1–8] or effective methods to remove CO_2 from DMFC [9,10]. Some conducted experimental study about formation of CO_2 bubbles on the surface of gas diffusion layer and slug elongation, movement through the channel by using different manifold designs or gas diffusion layers in order to find better anode flow field for good removal of CO_2. Relatively few numerical studies focusing on CO_2 in DMFC have been published [11–14].

Argyropoulos et al. [1] stressed importance of CO_2 gas management by conducting a visualizing experimental study using two DMFCs with different flow field designs. Lu et al. [2] observed that the pattern of CO_2 bubble generation is different according GDL material type by conducting experiments with two kinds of MEA with transparent cells for flow visualization. Following Lu et al. [2], Yang et al. [3] conducted further visualization study of CO_2 behavior by placing a DMFC in three different directions (vertical, anode-above MEA, anode-below MEA). They concluded vertical direction is best for cell performance because buoyancy force assists the removal of gas bubbles in the anode channel. In their succeeding paper [4], they conducted a parametrical study focusing on the

* Corresponding author. Present affiliation: LG Chem Research Park, Battery R&D, Address: 104-1, Moonji-dong, Yuseong-gu, Daejeon, 305-380, Republic of Korea, Tel.: +82 42 866 2094; fax: +82 42 862 1981.
E-mail addresses: stratus760@gmail.com (S. Jung), yul10@psu.edu (Y. Leng), cxw31@psu.edu (C.-Y. Wang).
[1] Contributing author info. Primary telephone number: +1-814-863-0749 Primary fax number: Present affiliation: Electrochemical Engine Center, Department of Mechanical and Nuclear Engineering, The Pennsylvania State University Address: The Pennsylvania State University, University Park, PA 16802, USA
[2] Contributing author info. Primary telephone number: +1-814-863-4762 Present affiliation: Electrochemical Engine Center, Department of Mechanical and Nuclear Engineering, The Pennsylvania State University Address: The Pennsylvania State University, University Park, PA 16802, USA

http://dx.doi.org/10.1016/j.electacta.2014.04.087
0013-4686/

Nomenclature

Acronyms and abbreviations

A	area (m^2)
a_s	specific reaction area (m^{-1})
c	molar concentration ($mol\,m^{-3}$)
D	diffusivity ($m^2\,s^{-1}$)
E^0	thermodynamic reversible voltage (V)
g	Gibbs free energy ($kJ\,kg^{-1}$)
gdl, GDL	gas diffusion layer
h	enthalpy ($kJ\,kg^{-1}$)
i	current density ($A\,m^{-2}$ or $mA\,cm^{-2}$)
I	current (A)
$\underline{j}$	volumetric transfer current density ($A\,m^{-3}$)
j	phase diffusion flux ($mol\,m^{-2}s^{-1}$),
K	permeability (m^2)
k_a	anode kinetics coefficient
k_H	Henry's constant
m	mass (kg)
L	length (m)
M	molar weight ($g\,mol^{-1}$)
N	molar flux ($mol\,m^{-2}s^{-1}$)
p	pressure (Pa)
n_d	electro-osmosis drag coefficient
s	liquid saturation
S	volumetric source term
u	velocity ($m\,s^{-1}$)
T	temperature (K)
V	volume (m^3)
X	species mole fraction
Y	species mass fraction

Greek letters

α	water transfer coefficient
δ	thickness (m)
ε	porosity
ϕ	potential (V)
γ	advection correction factor
η	overpotential
κ	ionic conductivity ($S\,cm^{-1}$)
λ	mobility, water content
μ	viscosity ($kg\,m^{-1}s^{-1}$)
ν	kinetic viscosity ($m^2\,s^{-1}$)
θ	contact angle (°)
ρ	density ($kg\,m^{-3}$)
τ	shear stress (Pa)
ξ	efficiency
ζ	stoichiometry

Superscript and subscript

a	anode
acl	anode catalyst layer
adl	anode gas diffusion layer
c	cathode
ccl	cathode catalyst layer
cdl	cathode gas diffusion layer
capill	capillary
d	drag
diff	diffusion
e	electrolyte phase
eff	effective
g	gas
k	species
l	liquid
mem	membrane
ref	reference
s	solid phase
tot	total
xover	crossover

effect of anode flow field design on cell performance. Mench et al. [5] observed gas bubble emergence/detachment on the surface of gas diffusion layer with video microscopy. Bewer et al. [6] devised a unique method to simulate CO_2 bubble behavior in anode flow field using H_2O_2 solution without actual DMFC equipment. Liao et al. [7] studied the dynamic behavior of CO_2 gas bubbles by using a transparent cell. Wong et al. [8] conducted further study about the dynamic behavior of CO_2 gas bubbles in anode channel. They examined the residence time of CO_2 bubbles in anode channel by changing the channel size and found that gas slug size and residence time increase with reduction of anode channel size. Scott et al. [9] studied the feasibility of using stainless steel mesh material as flow beds for DMFC in order to facilitate CO_2 removal. However, their cell didn't show significant performance improvement even though it was operated at 90 °C. Lundin et al. [10] introduced a unique method to reduce CO_2 bubble formation in the anode channel by adding chemical agents like LiOH or KOH which increase CO_2 solubility to liquid fuel mixture. However, they didn't mention possible adverse consequences which may occur by adding such alkaline agents into fuel.

In order to overcome problems caused by CO_2 flow in the anode channel, several methods have been suggested. MTI Microfuel Cells Inc. claimed two patents about CO_2 separation method. One uses gas permeable/liquid impermeable membrane which covers anode channels [15]. The other removes CO_2 through the composite membrane which plays as both proton conducting membrane and CO_2 separator [16]. Both cell designs remove CO_2 gas directly to the ambient, not through the anode channel. This is different from the conventional method which requires CO_2 separator outside of the cell. By adopting this kind of CO_2 removal method, the DMFC system can become very compact. Meng and Kim [17] developed a unique cell design which uses produced CO_2 as the driving force delivering liquid fuel. CO_2 is finally removed from the anode channel to the ambient through porous membrane in their cell. When a DMFC directly vents CO_2 gas to the ambient, it is called 'CO_2 breathing DMFC'.

Fig. 1(b) shows a schematic of a CO_2 breathing DMFC designed for the present study. By attaching a gas-permeable/liquid-impermeable membrane (surface film) such as PTFE film on the top of the anode bipolar plate, CO_2 can be directly removed to the ambient. Depending on the membrane property, CO_2 removal amount can be controlled. If gas-permeability is very high, almost pure liquid will flow through the anode channel. In order to prevent liquid water from leaking out of the cell, a dense hydrophobic porous layer made of ceramics may be used instead of surface film. However, CO_2 breathing cell requires more consideration to construct bipolar structure to combine CO_2 gas venting path and electrical connection together when cells form a stack structure.

2. Multi-dimensional DMFC model

The present multi-D model simulates steady-state cell operation under given condition and the model is extended from the work by Liu and Wang [18], and Jung [19,20]. Multi-D model consists of six coupled PDEs as summarized in Table 1. Constitutive relationships and parameters used in the present model are listed in Table 2. A detail derivation of governing equations is found in

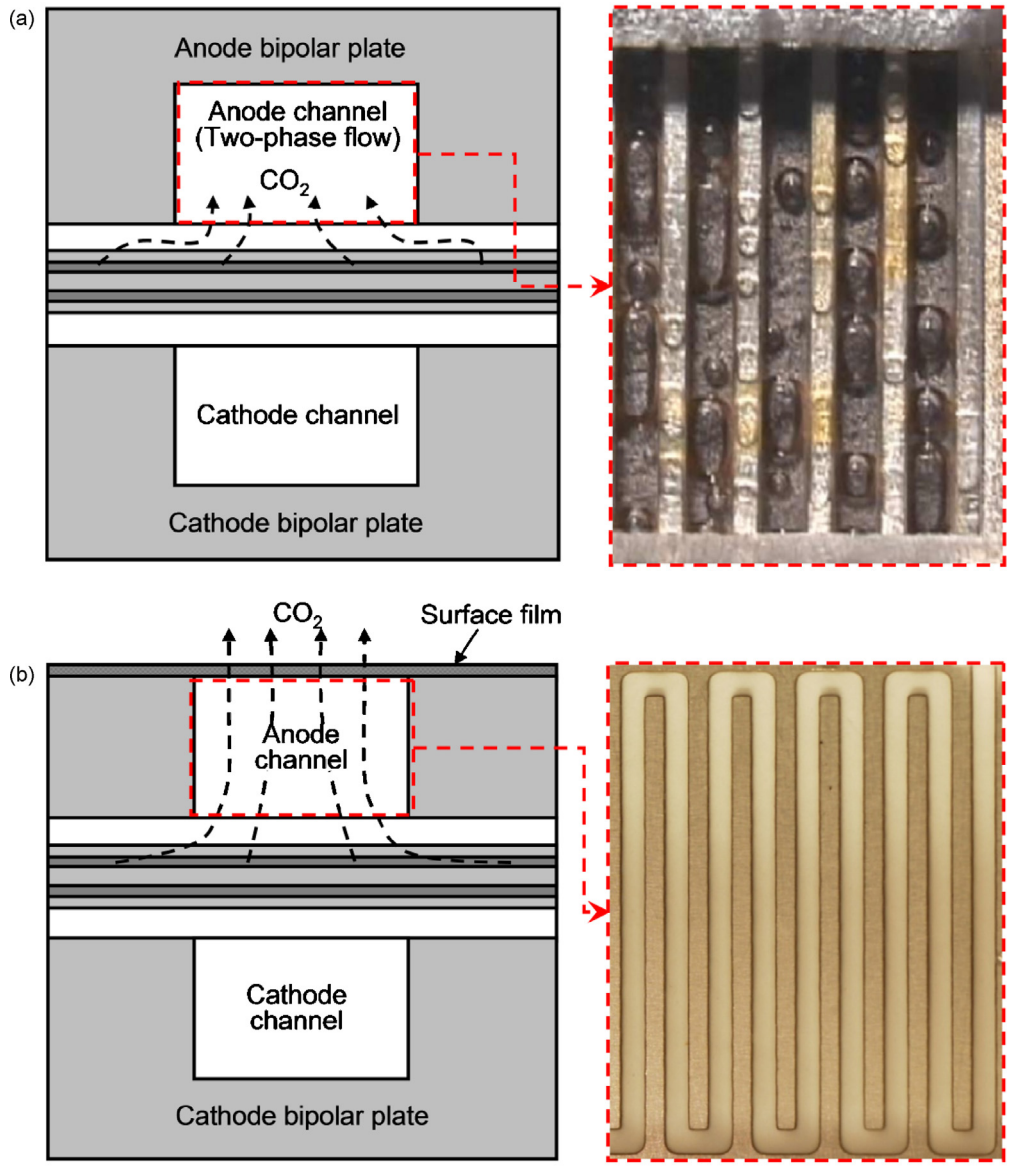

Fig. 1. (a) Schematic of the conventional DMFC showing CO_2 removal route and two-phase flow in anode channel [2], (b) Schematic of the CO_2 breathing DMFC showing CO_2 removal route and almost pure liquid flow in anode channel without CO_2 bubbles (present study).

Table 1
Governing equations of the multi-D DMFC model.

	Conservation equations	Source terms
Mass	$\nabla\cdot(\rho\vec{u}) = S^m$	$S^m_{\text{acl}} = M^{\text{MeOH}}S^{\text{MeOH}} + M^{\text{H}_2\text{O}}S^{\text{H}_2\text{O}} + \frac{j}{6F}M^{\text{CO}_2}$
		$S^m_{\text{ccl}} = M^{\text{H}_2\text{O}}S^{\text{H}_2\text{O}} + M^{\text{O}_2}S^{\text{O}_2} + \frac{j_{\text{xover}}}{6F}M^{\text{CO}_2}$
Momentum	$\nabla\cdot\left(\rho\vec{u}\vec{u}\right) = -\nabla p + \nabla\cdot\vec{\tau} + S^{\text{u}}$	$S^{\text{u}} = -\frac{\mu}{K}\vec{u}$ (in porous media domain)
Water transport	$\nabla\cdot\left(\gamma\rho\vec{u}Y^{\text{H}_2\text{O}}\right) = \nabla\cdot\left[\rho D_{\text{capill}}\nabla Y^{\text{H}_2\text{O}}\right] + S^{\text{H}_2\text{O}}$	$S^{\text{H}_2\text{O}}_{\text{acl}} = -\frac{j}{6F}M^{\text{H}_2\text{O}} - \frac{j}{F}\alpha M^{\text{H}_2\text{O}}$
		$S^{\text{H}_2\text{O}}_{\text{ccl}} = \frac{j}{2F}M^{\text{H}_2\text{O}} + \frac{j_{\text{xover}}}{3F}M^{\text{H}_2\text{O}} + \frac{j}{F}\alpha M^{\text{H}_2\text{O}}$
Methanol transport	$\nabla\cdot\left(\gamma\rho\vec{u}Y^{\text{MeOH}}_{\text{l}}\right) = \nabla\cdot\left[\rho D^{\text{MeOH}}_{\text{eff}}\nabla\cdot Y^{\text{MeOH}}_{\text{l}}\right] + S^{\text{MeOH}}$	$S^{\text{MeOH}}_{\text{acl}} = -\frac{j}{6F}M^{\text{MeOH}} - \frac{j_{\text{xover}}}{6F}M^{\text{MeOH}}$
CO_2 transport	$\nabla\cdot\left(\gamma\rho\vec{u}Y^{\text{CO}_2}\right) = \nabla\cdot\left[\rho\left(\frac{\rho_{\text{g}}}{\rho}D^{\text{CO}_2}_{\text{g,eff}}\right)\nabla Y^{\text{CO}_2}\right] + \nabla\cdot\left[Y^{\text{CO}_2}\vec{j}_{\text{l}}\right] + S^{\text{CO}_2}$	$S^{\text{CO}_2}_{\text{acl}} = \frac{j}{6F}M^{\text{CO}_2}$
		$S^{\text{CO}_2}_{\text{ccl}} = \frac{j_{\text{xover}}}{6F}M^{\text{CO}_2}$
Oxygen transport	$\nabla\cdot\left(\gamma\rho\vec{u}Y^{\text{O}_2}\right) = \nabla\cdot\left[\rho\left(\frac{\rho_{\text{g}}}{\rho}D^{\text{O}_2}_{\text{g,eff}}\right)\nabla Y^{\text{O}_2}\right] + \nabla\cdot\left[Y^{\text{O}_2}\vec{j}_{\text{l}}\right] + S^{\text{O}_2}$	$S^{\text{O}_2}_{\text{ccl}} = -\frac{j}{4F}M^{\text{O}_2} - \frac{j_{\text{xover}}}{4F}M^{\text{O}_2}$
Proton	$0 = \nabla\cdot(\kappa_{\text{e,eff}}\nabla\phi_{\text{e}}) + S^{\phi}_{\text{e}}$	$S^{\phi}_{\text{e,acl}} = j$
		$S^{\phi}_{\text{e,ccl}} = -j_{\text{c}} + j_{\text{xover}}$
Electron	$0 = \nabla\cdot(\kappa_{\text{s,eff}}\nabla\phi_{\text{s}}) + S^{\phi}_{\text{s}}$	$S^{\phi}_{\text{s,acl}} = -j$
		$S^{\phi}_{\text{s,ccl}} = j_{\text{c}} - j_{\text{xover}}$

Table 2
Constitutive relationships and parameters for DMFC model.

Parameters	Expression	Reference
Relative permeability	$k_{rl} = s^n$; $k_{rg} = (1-s)^n$	[27]
Methanol diffusivity (vapor)	$D_g^{MeOH} = 1.96\times10^{-5}\left(\frac{T}{328.15}\right)^{1.823}\frac{1.013\times10^5}{p}$	[28]
Water diffusivity (vapor)	$D_g^{H_2O} = 2.01\times10^{-5}\left(\frac{T}{307}\right)^{1.823}\frac{1.013\times10^5}{p}$	[29]
Methanol diffusivity (liquid)	$D_l^{MeOH} = 1.4\times10^{-9}\left(\frac{647.3-298.15}{647.3-T}\right)^6$	[29,30]
Oxygen diffusivity (gas)	$D_g^{O_2} = 3.57\times10^{-5}\left(\frac{T}{352}\right)^{1.823}\frac{1.013\times10^5}{p}$	[29]
Water content in Nafion-membrane	$\lambda = \begin{cases} 22 & (s>0.3) \\ 14+8s/0.3 & (s\le 0.3) \\ 0.043+17.81RH-39.85RH^2+36.0RH^3 & (\text{vapor}) \end{cases}$	[31,32]
Water diffusivity in Nafion-membrane	$D_{mem}^{H_2O} = 4.80\times10^{-11}\exp\left[2416\left(\frac{1}{303}-\frac{1}{T}\right)\right]$	Calibrated based on [32]
Methanol diffusivity in Nafion-membrane	$D_{mem}^{MeOH} = 1.5\times10^{-10}\exp\left[2416\left(\frac{1}{303}-\frac{1}{T}\right)\right]$	Calibrated based on [32]
Water EOD coefficient in Nafion-membrane	$n_d^{H_2O} = \begin{cases} \left[\frac{\lambda-14}{8}\right]\left(n_{d,ref}^{H_2O}-1\right)+1 & (\text{for}\lambda\ge14) \\ 1 & (\text{for}\lambda<14) \end{cases}$	[33], [34]
Water reference EOD coefficient in Nafion-membrane	$n_{d,ref}^{H_2O} = 1.6767+0.0155(T-273)+8.9074\times10^{-5}(T-273)^2$	[33]
Ion conductivity of Nafion-membrane	$\kappa_{mem} = 0.1\,(\text{S cm}^{-1})$@60°C (fully hydrated)	
Effective water vapor diffusivity	$D_{g,eff}^{H_2O} = D_g^{H_2O}(1-s)^n\varepsilon^n$	
Effective water liquid diffusivity	$D_{l,eff}^{H_2O} = D_l^{H_2O}s^n\varepsilon^n$	
J - Leverett function	$J(s) = \begin{cases} -1.263s^3+1.669s^2-0.966s+0.56 & (\text{when}\ \theta_c<90^\circ) \\ 1.263s^3-2.120s^2+1.417s & (\text{when}\ \theta_c>90^\circ) \end{cases}$	
Henry's constant of methanol	$k_H^{MeOH} = \frac{160.0}{101.235}\exp\left[4210\left(\frac{1}{T}-\frac{1}{298.15}\right)\right]\frac{R}{T}$	Fitted data

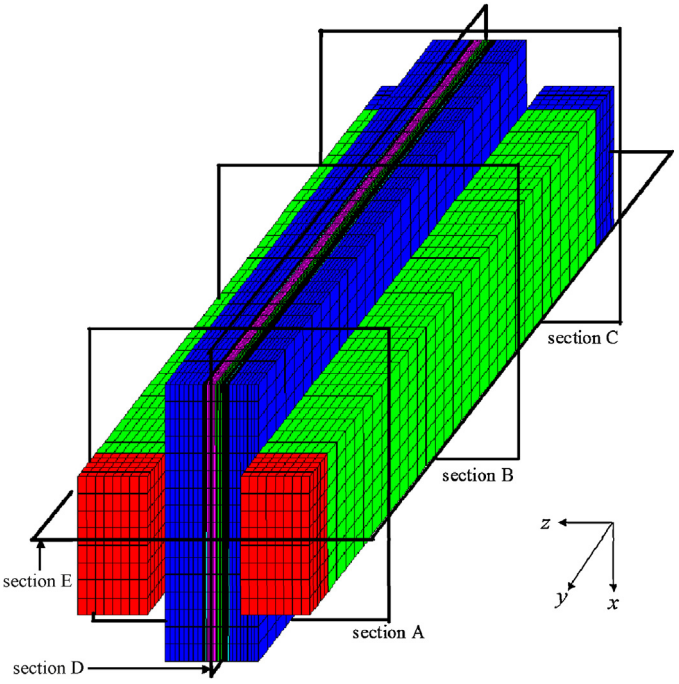

Fig. 2. Three-dimensional geometry of the present DMFC model.

Table 3
Cell geometry and material properties.

Description	Symbol	Value
Anode gas diffusion layer thickness	δ_{adl}	170 μm
Anode catalyst layer thickness	δ_{acl}	30 μm
Membrane thickness	δ_{mem}	50 μm
Cathode catalyst layer thickness	δ_{ccl}	30 μm
Cathode gas diffusion layer thickness	δ_{cdl}	200 μm
Gas diffusion layer porosity	ε_{gdl}	0.6
Catalyst layer porosity	ε_{cl}	0.4
Gas diffusion layer permeability	K_{gdl}	2.0×10^{-12} m^2
Catalyst layer permeability	K_{cl}	1.0×10^{-13} m^2
Membrane permeability	K_{mem}	2.0×10^{-20} m^2
Gas diffusion layer contact angel	θ_{gdl}	110°
Catalyst layer contact angle	θ_{cl}	100°
Cell length	L_{cell}	75 mm
Channel width	W_{chn}	1 mm
Channel height	H_{chn}	0.5 mm
Land width	W_{land}	1 mm
Bipolar plate thickness	H_{bp}	0.5 mm

Table 4
Baseline simulation parameters.

Description	Symbol	Value
Cell temperature	T_{cell}	313 K
Reference current density	i_{ref}	150 mA cm^{-2}
Anode stoichiometry	ξ_a	3
Cathode stoichiometry	ξ_c	3
Anode exchange current density	$i_{0,a}$	45.51 A m^{-2}
Cathode exchange current density	$i_{0,c}$	0.12 A m^{-2}
Anode catalyst ionomer		25 vol.%
Cathode catalyst ionomer		25 vol.%
Anode catalyst loading		4 mg cm^{-2}
Cathode catalyst loading		2 mg cm^{-2}
Surface tension	σ	0.0625 N m^{-1}
Inlet methanol concentration	c_{in}^{MeOH}	2000 mol m^{-3}
Pure MeOH concentration	$c_{l,pure}^{MeOH}$	24719 mol m^{-3}
Pure H_2O concentration	$c_{l,pure}^{H_2O}$	55556 mol m^{-3}
Anode transfer coefficients	α_a	0.239
Cathode transfer coefficients	α_c	0.875
Faraday constant	F	96487 C mol^{-1}
Universal gas constant	R	8.314 J mol^{-1} K^{-1}
Equivalent weight of dry membrane	EW	1.1 kg mol^{-1}
Dry membrane density	ρ_{dry}	1980 kg m^{-3}

the references [18–20]. Present study focuses on the role of CO_2 in two-phase transport of water and methanol in a DMFC. Fig. 2 and Table 3 shows the three-dimensional model geometry. Baseline simulation parameters are listed in Table 4. All derived sets of governing equations, parameters and constitutional relations are implemented into commercial CFD solver, STAR-CD®. AMG (algebraic multi-grid method) based on finite volume method (FVM) is used for discretization and SIMPLE algorithm is applied for solving governing equations. It is considered that convergence is achieved when the residuals reach 10^{-8}.

2.1. Two-phase water transport and the relationship with CO_2

A general form of the multi-phase species equation by M^2 model [21] which is the base of the present multi-D model is expressed as follows:

$$\nabla\cdot(\gamma\rho\vec{u}Y^{k}) = \nabla\cdot\left[\rho_{l}D^{k}_{l,\mathrm{eff}}\nabla Y^{k}_{l} + \rho_{g}D^{k}_{g,\mathrm{eff}}\nabla Y^{k}_{g}\right] - \nabla\cdot\left[\left(Y^{k}_{l}-Y^{k}_{g}\right)\vec{j}_{l}\right] + S^{k} \quad (1)$$

Capillary flux of liquid phase ($\vec{j}$) shown above equation is driven by capillary pressure gradient ($\nabla p_{\mathrm{capill}}$) and it can be expressed by Darcy's law as follows:

$$\vec{j}_{l} = \frac{\lambda_{g}\lambda_{l}K}{\nu}\nabla p_{\mathrm{capill}} = \frac{\lambda_{g}\lambda_{l}K}{\nu}\nabla\left[\sigma\cos(\theta)\left(\frac{\varepsilon}{K}\right)^{1/2}J(s)\right] = \frac{\lambda_{g}\lambda_{l}\sigma\cos(\theta)(K\varepsilon)^{1/2}}{\nu}\frac{dJ}{ds}\nabla s \quad (2)$$

where the liquid saturation is defined as

$$s = \frac{V_{l}}{V_{\mathrm{pore}}} = 1-\frac{V_{g}}{V_{\mathrm{pore}}} = \frac{\rho_{g}\left(1-Y^{CO_2}\right)}{\rho_{l}Y^{CO_2}+\rho_{g}\left(1-Y^{CO_2}\right)} \quad (3)$$

Now, capillary flux ($\vec{j}_{l}$) is expressed as a function of liquid saturation, and the liquid saturation is strongly affected by the CO_2 fraction in Eq. (3) since large amount of gas in the anode consists of CO_2. Therefore, it is conjectured that the capillary flux in the anode is controlled by CO_2. In addition, it can be easily conjectured that large amount of CO_2 in the anode will lead to lower water crossover to the cathode side by building dry condition in the anode porous media. CO_2 amount in the anode is defined as CO_2 level as follows in the present study.

$$\mathrm{CO_2Level} = \int_{V}\left\{\frac{\rho_{g}(1-s)}{\sum_{i}^{n}M^{i}X^{i}}\left(1-\frac{c^{H_2O}_{sat}M^{H_2O}}{\rho^{H_2O}_{g}}-\frac{c^{MeOH}_{l}M^{MeOH}}{\rho^{MeOH}_{g}k_{H}}\right)\right\}dV \quad [\mathrm{mol/m^3}] \quad (4)$$

By plugging Eq. (3) into Eq. (2), capillary diffusive flux can be reformed as follows:

$$\vec{j}_{l} = \frac{\lambda_{g}\lambda_{l}\sigma\cos(\theta)(K\varepsilon)^{1/2}}{\nu}\frac{dJ}{ds} \times \frac{\rho_{l}\left(\rho_{g}Y^{H_2O}_{l}-\rho_{g}Y^{H_2O}_{g}\right)}{\left(\rho_{l}Y^{H_2O}_{l}-\rho_{l}Y^{H_2O}+\rho_{g}Y^{H_2O}-\rho_{g}Y^{H_2O}_{g}\right)^{2}}\nabla Y^{H_2O} \quad (5)$$

Now, water transport equation can be derived by plugging Eq. (5) into Eq. (1) as follows:

$$\nabla\cdot\left(\gamma\rho\vec{u}Y^{H_2O}\right) = \nabla\cdot\left[\rho D_{\mathrm{capill}}\nabla Y^{H_2O}\right] + S^{H_2O} \quad (6)$$

where capillary diffusivity is

$$D_{\mathrm{capill}} = \frac{1}{\rho}\left(Y^{H_2O}_{l}-Y^{H_2O}_{g}\right)\frac{\lambda_{g}\lambda_{l}\sigma\left|\cos(\theta)\right|(K\varepsilon)^{1/2}}{\nu}\frac{dJ}{ds} \times \frac{\rho_{l}\left(\rho_{g}Y^{H_2O}_{l}-\rho_{g}Y^{H_2O}_{g}\right)}{\left(\rho_{l}Y^{H_2O}_{l}-\rho_{l}Y^{H_2O}+\rho_{g}Y^{H_2O}-\rho_{g}Y^{H_2O}_{g}\right)^{2}} \quad (7)$$

Capillary diffusivity shown above is a complex function of material properties (porosity, permeability, and contact angle), species composition, and liquid saturation.

2.2. Two-phase methanol transport and the relationship with CO_2

Assuming the vapor-liquid equilibrium of methanol in the anode, the methanol concentration can be related by Henry's law as follows:

$$c^{MeOH}_{l} = c^{MeOH}_{g}k^{MeOH}_{H}$$

where

$$k^{MeOH}_{H} = \frac{160.0}{101.235}\exp\left[4210\left(\frac{1}{T}-\frac{1}{298.15}\right)\right]\frac{R}{T} \quad (8)$$

Two-phase mixture of methanol mass fraction can be expressed as the following by the multi-phase mixture model [21].

$$\rho Y^{MeOH} = \rho_{l}Y^{MeOH}_{l}s + \rho_{g}Y^{MeOH}_{g}(1-s) \quad \text{where} \quad \begin{cases}\rho Y^{MeOH} = c^{MeOH}M^{MeOH}\\ \rho_{l}Y^{MeOH}_{l} = c^{MeOH}_{l}M^{MeOH}\\ \rho_{g}Y^{MeOH}_{g} = c^{MeOH}_{g}M^{MeOH}\end{cases} \quad (9)$$

In order to solve methanol governing equation the above Eq. (8) is converted in term of methanol mass fraction using Eq. (9) as

$$Y^{MeOH} = \frac{\rho_{l}}{\rho}\left(s+\frac{1-s}{k_{H}}\right)Y^{MeOH}_{l} \quad (10)$$

Now, the species equation (Eq. (1)) which has three variables of methanol (Y^{MeOH}, Y^{MeOH}_{l}, Y^{MeOH}_{g}) is summarized as the following equation with a single variable (Y^{MeOH}), which is mathematically easy to solve.

$$\nabla\cdot\left(\rho\vec{u}Y^{MeOH}_{l}\right) = \nabla\cdot\left[\rho_{l}\left(D^{MeOH}_{l,\mathrm{eff}}+\frac{D^{MeOH}_{g,\mathrm{eff}}}{k_{H}}\right)\nabla\cdot Y^{MeOH}_{l}\right] - \nabla\cdot\left[\left(Y^{MeOH}_{l}-Y^{MeOH}_{g}\right)\vec{j}_{l}\right] + S^{MeOH} \quad (11)$$

Examining the above methanol transport equation, left term is advection term which is dominant in the channel flow region. The first term on the right hand side expresses the molecular diffusion which is conducted by both liquid-phase and gas-phase. Therefore, the two-phase molecular diffusivity can be defined as follows [20]:

$$D^{MeOH}_{mol} = \frac{\rho_{l}}{\rho}\left(D^{MeOH}_{l,\mathrm{eff}}+\frac{D^{MeOH}_{g,\mathrm{eff}}}{k_{H}}\right) = \frac{\rho_{l}}{\rho}\left(D^{MeOH}_{l}s^{n}+\frac{D^{MeOH}_{g}(1-s)^{n}}{k_{H}}\right)\varepsilon^{n} \quad (12)$$

Two-phase molecular diffusivity of methanol is a strong function of liquid saturation, and porosity as shown in Fig. 3. The second term on the right hand side of Eq. (11) represents capillary diffusion of methanol, which is difficult to deal with as it is. We transform this term to a unified diffusive term as follows: First, combining Eq. (5) and Eq. (7), liquid phase flux becomes,

$$\vec{j}_{l} = \frac{\rho D_{\mathrm{capill}}}{Y^{H_2O}_{l}-Y^{H_2O}_{g}}\nabla Y^{H_2O} \quad (13)$$

Therefore, methanol capillary term becomes,

$$S^{MeOH}_{\mathrm{capill}} = -\nabla\cdot\left[\left(Y^{MeOH}_{l}-Y^{MeOH}_{g}\right)\vec{j}_{l}\right] = \nabla\cdot\left[Y^{MeOH}_{l}\left(\frac{\rho_{l}}{\rho_{g}k_{H}}-1\right)\vec{j}_{l}\right] = -\nabla\cdot\left[Y^{MeOH}_{l}\left(1-\frac{\rho_{l}}{\rho_{g}k_{H}}\right)\frac{\rho D_{\mathrm{capill}}}{Y^{H_2O}_{l}-Y^{H_2O}_{g}}\nabla Y^{H_2O}\right] = \nabla\cdot\left[\rho\nabla D^{MeOH}_{\mathrm{capill}}Y^{MeOH}_{l}\right] \quad (14)$$

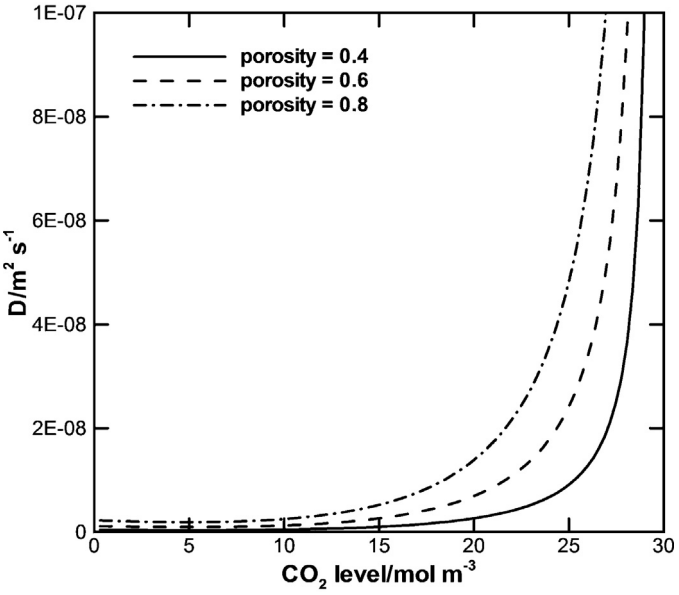

Fig. 3. Molecular diffusivity of methanol in gas diffusion layer according to CO_2 level and porosity of gas diffusion layer.

Methanol capillary diffusivity in the above equation is expressed as:

$$D_{\text{capill}}^{\text{MeOH}} = D_{\text{capill}}\psi$$

$$\text{where} \quad \psi = \left(1 - \frac{\rho_{\text{l}}}{\rho_{\text{g}} k_{\text{H}}}\right) \frac{Y_{\text{l}}^{\text{MeOH}}}{Y_{\text{l}}^{\text{H}_2\text{O}} - Y_{\text{g}}^{\text{H}_2\text{O}}} \tag{15}$$

In the above equation, CO_2 level affects liquid phase capillary diffusivity (D_{capill}) whereas cell temperature and methanol concentration strongly affects methanol capillary factor (ψ). Fig. 4 shows that the methanol capillary factor becomes large when the liquid mixture is highly concentrated and temperature is low. However, even though methanol capillary factor is high, methanol capillary diffusivity may remain low if the cell operates at very low flow stoichiometry. This is because liquid phase diffusivity becomes very low under such a gaseous condition (or high CO_2 level environment). In contrast, there will be no methanol capillary diffusion also if the porous media is filled with pure liquid. Finally, the methanol transport equation becomes,

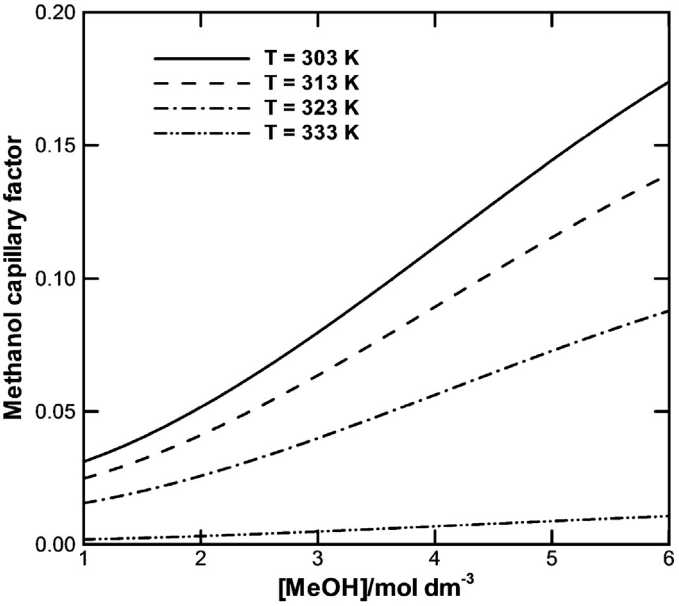

Fig. 4. Methanol capillary factor according to temperature and methanol concentration.

$$\nabla \cdot \left(\rho \vec{u} Y_{\text{l}}^{\text{MeOH}}\right) = \nabla \cdot \left[\rho D_{\text{eff}}^{\text{MeOH}} \nabla \cdot Y_{\text{l}}^{\text{MeOH}}\right] + S^{\text{MeOH}} \tag{16}$$

The effective methanol diffusivity in the above equation is,

$$D_{\text{eff}}^{\text{MeOH}} = D_{\text{mol}}^{\text{MeOH}} + D_{\text{capill}}^{\text{MeOH}} \tag{17}$$

It is important to identify which transport physics dominates in fuel delivery in order to control fuel delivery and optimize the anode design under given operational condition. For example, under ultra-low anode flow rate condition, the anode becomes very gaseous and fuel delivery is dominated by molecular diffusion.

2.3. Net water transfer coefficient (α)

In order to express water transport through the membrane, the net water transport coefficient (α) was introduced [22]. This coefficient consists of electro-osmosis drag, diffusion and hydraulic permeation as shown in Eq. (18). Positive α value means water in the anode is being lost by the cathode whereas negative α value indicates water on the cathode side moves to the anode side.

$$\begin{aligned} \alpha &= N_{\text{mem}}^{\text{H}_2\text{O}} \frac{F}{i} = (N_{\text{mem,EOD}}^{\text{H}_2\text{O}} + N_{\text{mem,diff}}^{\text{H}_2\text{O}} + N_{\text{mem,pl}}^{\text{H}_2\text{O}}) \frac{F}{i} \\ &= n_{\text{d}}^{\text{H}_2\text{O}} + \alpha_{\text{mem,diff}} + \alpha_{\text{mem,pl}} \end{aligned}$$

$$\text{where} \begin{cases} n_{\text{d}}^{\text{H}_2\text{O}} = N_{\text{m,EOD}}^{\text{H}_2\text{O}} \dfrac{F}{i} \\ \alpha_{\text{m,diff}} = N_{\text{m,diff}}^{\text{H}_2\text{O}} \dfrac{F}{i} = D_{\text{mem}}^{\text{H}_2\text{O}} \left(\dfrac{\rho_{\text{mem}}}{EW_{\text{mem}}}\right) \left(\dfrac{\lambda_{\text{a}} - \lambda_{\text{c}}}{\delta_{\text{mem}}}\right) \dfrac{F}{i} \\ \alpha_{\text{m,pl}} = N_{\text{m,pl}}^{\text{H}_2\text{O}} \dfrac{F}{i} = \left(\dfrac{\rho_{\text{l}} K_{\text{mem}}}{M_{\text{l}} \mu_{\text{l}}}\right) \left(\dfrac{p_{\text{l,a}} - p_{\text{l,c}}}{\delta_{\text{mem}}}\right) \dfrac{F}{i} \end{cases} \tag{18}$$

2.4. MOR and ORR

When methanol concentration is high it is believed that methanol oxidation reaction (MOR) is 0^{th} order whereas MOR becomes 1^{st} order as the methanol concentration approaches the depletion limit. Eq. (19) proposed by Meyers and Newman [23–25] is used to capture MOR transition from 0^{th} order to 1^{st} order in this study.

$$j_{\text{a}} = a_{\text{s}} i_{0,\text{a}} \left(\frac{c_{\text{acl}}^{\text{MeOH}} \exp(\frac{\alpha_{\text{a}} F}{RT} \eta_{\text{a}})}{c_{\text{acl}}^{\text{MeOH}} + k_{\text{a}} \exp(\frac{\alpha_{\text{a}} F}{RT} \eta_{\text{a}})} \right)$$

$$\text{where} \quad \eta_{\text{a}} = \phi_{\text{s}} - \phi_{\text{e}} - E_{\text{a}}^0 \tag{19}$$

Note k_{a} is a reaction constant to smoothly fit the MOR transition from 0^{th} order to 1^{st} order, which is 0.2 in this study.

Oxygen reduction reaction (ORR) in the cathode is expressed as Eq. (20) which is based on Tafel equation. Note $(1\text{-}s)^n$ is multiplied to consider flooding effect in the cathode.

$$j_c = a_{\text{s}} i_{0,\text{c}} \left(\frac{c_{\text{ccl}}^{\text{O}_2}}{c_{\text{ref}}^{\text{O}_2}} \right) (1 - s)^n \exp\left(-\frac{\alpha_{\text{c}} F}{RT} \eta_{\text{c}}\right)$$

$$\text{where} \quad \eta_{\text{c}} = \phi_{\text{s}} - \phi_{\text{e}} - E_{\text{c}}^0 \tag{20}$$

2.5. Crossover current

Instead of participating in MOR, some amount of methanol in the anode permeates the membrane by electro-osmosis drag or

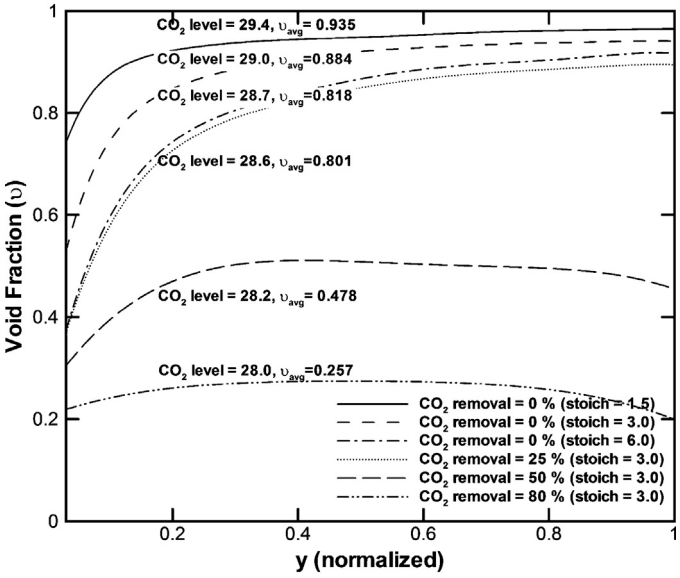

Fig. 5. Void fraction in the anode channel according to anode stoichiometry and CO_2 surface removal rate (T_{cell} = 333 K, i = 150 mA cm^{-2}).

diffusion and produces crossover current (i_{xover}) as shown in Eq. (21) [18].

$$i_{xover} = 6FN_{mem}^{MeOH}$$

$$\text{where} \quad N_{mem}^{MeOH} = \frac{i_{xover}}{6F} = n_d^{MeOH}\frac{i}{F} + D_{mem}^{MeOH}\frac{c_{acl}^{MeOH}}{\delta_{mem}} \tag{21}$$

Electro-osmosis drag coefficient of methanol shown in the above equation is found by $n_d^{MeOH} = n_d^{H_2O}\left(c_l^{MeOH}/c_l^{H_2O}\right)$. The crossover current (i_{xover}) forms mixed potential which degrades the cell performance. In addition, the fuel efficiency of the cell deteriorates since crossovered methanol is wasted away.

2.6. CO_2 surface removal

In reality, CO_2 removal amount through the surface film can be controlled by the material properties of the surface film such as porosity, permeability, and hydrophobicity. Instead, the present study simulates CO_2 surface removal amount by applying a CO_2 species sink in the surface film. When this removal amount is zero, the model represents a conventional DMFC which removes all of CO_2 gas through the outlet port, whereas 100% amount of CO_2 surface removal represents the ideal CO_2 breathing DMFC which has a pure liquid flow in the anode channel.

3. Result and Discussion

3.1. CO_2 removal and pressure drop

In a conventional DMFC, produced CO_2 accumulates and void fraction increases in the channel direction. This two-phase flow causes a large pressure drop in the channel. The present multi-D model described here applies a homogeneous flow model in the anode flow channel. When CO_2 is directly removed to the ambient through the surface film, CO_2 accumulation is reduced and average liquid saturation increases. Channel void fraction according to anode flow stoichiometry and CO_2 removal amount are presented in Fig. 5. When CO_2 surface removal rate is large, channel void fraction becomes relatively uniform compared to the conventional cell. Fig. 6 and Fig. 7 show the liquid saturation distribution in the anode. Liquid saturation in the anode gas diffusion layer of the CO_2 breathing cell is very uniform compared to the conventional cell.

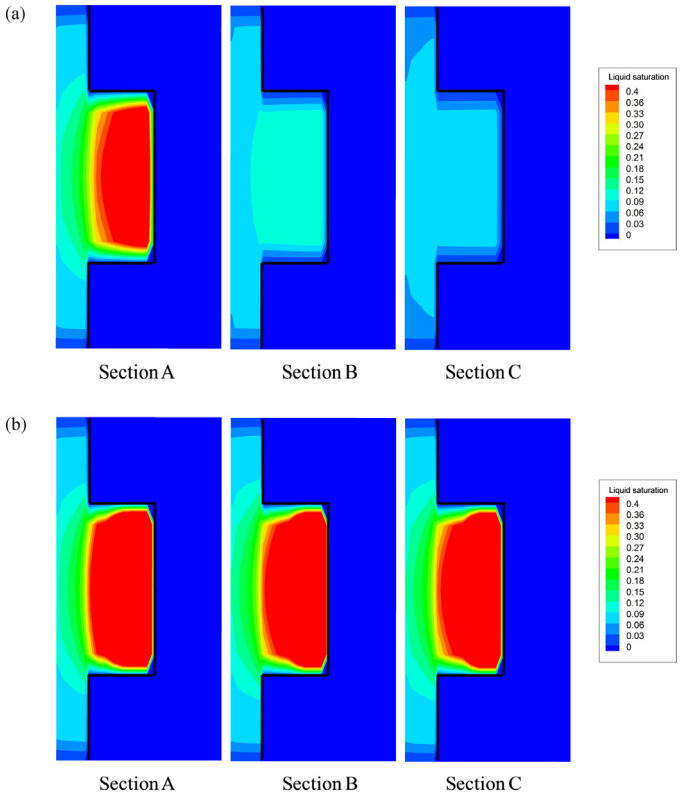

Fig. 6. Liquid saturation distribution in the anode: (a) Conventional DMFC, (b) CO_2 breathing DMFC (T_{cell} = 333 K, i = 150 mA cm^{-2}, ξ_a = 3.0, ξ_c = 3.0).

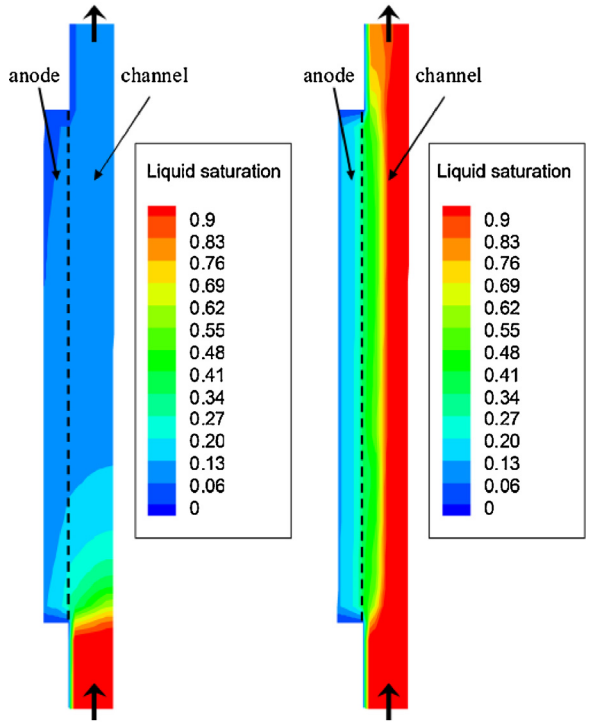

Fig. 7. Liquid saturation distribution in the anode (cross-section E in Fig. 2): (a) Conventional DMFC, (b) CO_2 breathing DMFC (T_{cell} = 333 K, i = 150 mA cm^{-2}, ξ_a = 3.0, ξ_c = 3.0).

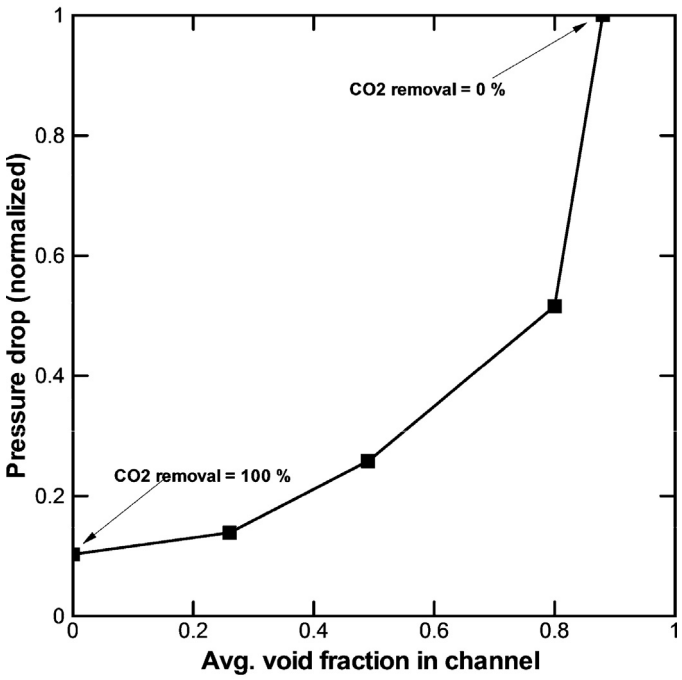

Fig. 8. Comparison of relative pressure drop according to average void fraction in the anode channel due to CO_2 surface removal. (T_{cell} = 333 K, i = 150 mA cm^{-2}, ξ_a = 3.0, ξ_c = 3.0).

By avoiding strong two-phase flow in the channel, pressure drop in the channel can be significantly reduced as shown in Fig. 8. It is estimated that the CO_2 breathing cell which completely removes CO_2 through the surface film requires only 10% of the pumping power of the conventional DMFC, which contributes to improving the new power throughput. In addition, reduced pumping power leads to smaller pump and reduced manufacturing cost.

3.2. Role of CO_2 in water management

Conventional cell shows gradually decreasing liquid saturation along the channel whereas the CO_2 breathing cell shows very uniform liquid saturation in the GDL since CO_2 is not accumulated (see Fig. 6 and Fig. 7). In other words, the CO_2 breathing cell has a wetter anode than the conventional cell. In both cases, the region under the anode land is gaseous (low liquid saturation) since CO_2 removal from the anode catalyst layer is blocked there. On the contrary, the region under the cathode land is quite wet (high liquid saturation) since water removal from cathode catalyst layer is blocked by the cathode land. Therefore, water back-diffusion strongly occurs under the land region, which leads to a lower local water transfer coefficient value there. Fig. 7 shows saturation distribution in a different view. Overall, the CO_2 breathing cell shows uniformly wetter anode porous media compared to the conventional cell since CO_2 surface removal occurs uniformly everywhere on the surface film, which implies that the CO_2 breathing cell has more uniform and larger water transfer coefficient than the conventional cell. Local water transfer coefficients of both cells are presented in Fig. 9. Conventional cell shows a large water transfer coefficient value at the inlet region where the anode is very wet and cathode is dry. In contrast, the CO_2 breathing cell shows relatively uniform distribution of water transfer coefficient value due to minimal CO_2 accumulation. This means more water is lost to the cathode than in the conventional cell. In both cells, the water transfer coefficient is low under the land region due to gaseous environment in the anode and wet environment in the cathode.

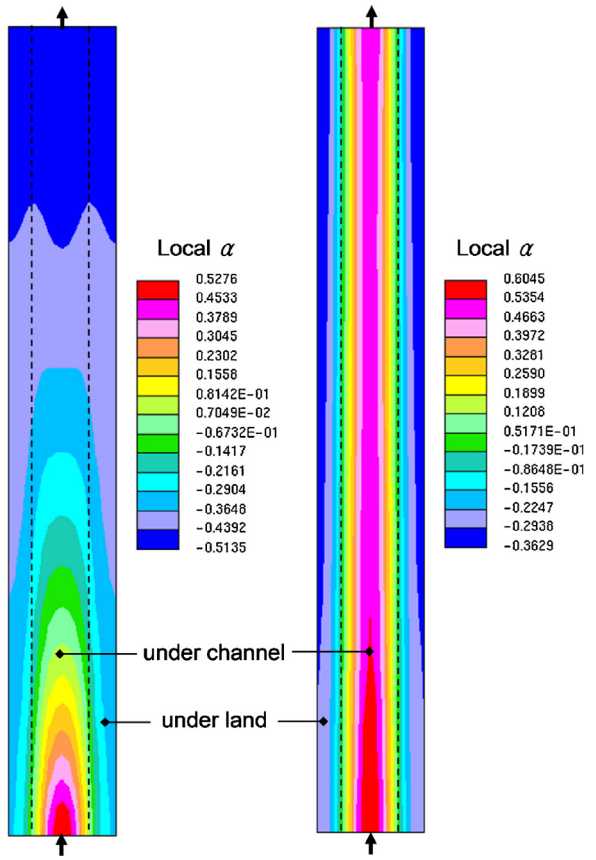

Fig. 9. Local water transfer coefficient distribution in the membrane: (a) Conventional DMFC, (b) CO_2 breathing DMFC (T_{cell} = 333 K, i = 150 mA cm^{-2}, ξ_a = 3.0, ξ_c = 3.0).

As the operating current density increases, the anode becomes more gaseous due to the large amount of CO_2 production by MOR in the anode catalyst layer as shown in Fig. 10(a) and, definitely, CO_2 level decreases as CO_2 surface removal increases. Fig. 10(b) shows that the water transfer coefficient becomes large as CO_2 level decreases or CO_2 surface removal increases. This simply implies that maintaining high CO_2 level helps to reduce the water transfer coefficient.

3.3. Role of CO_2 in methanol transport

Controlling methanol transport is important for steady operation of a DMFC. Too much methanol supply results in severe methanol crossover which degrades both cell performance and fuel efficiency. In contrast, the cell may shut down if too little methanol is delivered to the catalyst layer. As discussed, methanol is transported by molecular diffusion and capillary diffusion in the anode. CO_2 plays an important role for both two-phase transport mechanisms, depending on the cell operating condition such as flow rate, temperature and methanol concentration. Effective methanol diffusivity, consisting of two-phase molecular diffusivity and capillary diffusivity, expresses methanol delivery capability in anode porous media.

Methanol diffusivity analysis in the anode is shown in Fig. 11 according to cell temperature and CO_2 surface removal rate. CO_2 level affects the capillary diffusivity (see Eq. (7)) and cell temperature strongly affects methanol capillary factor (see Eq. (15)). When the cell operates at high temperature (T_{cell} = 333 K) without CO_2 surface removal (conventional DMFC), two-phase molecular diffusion is the dominant mechanism of methanol transport as shown in Fig. 11(a). Capillary diffusion

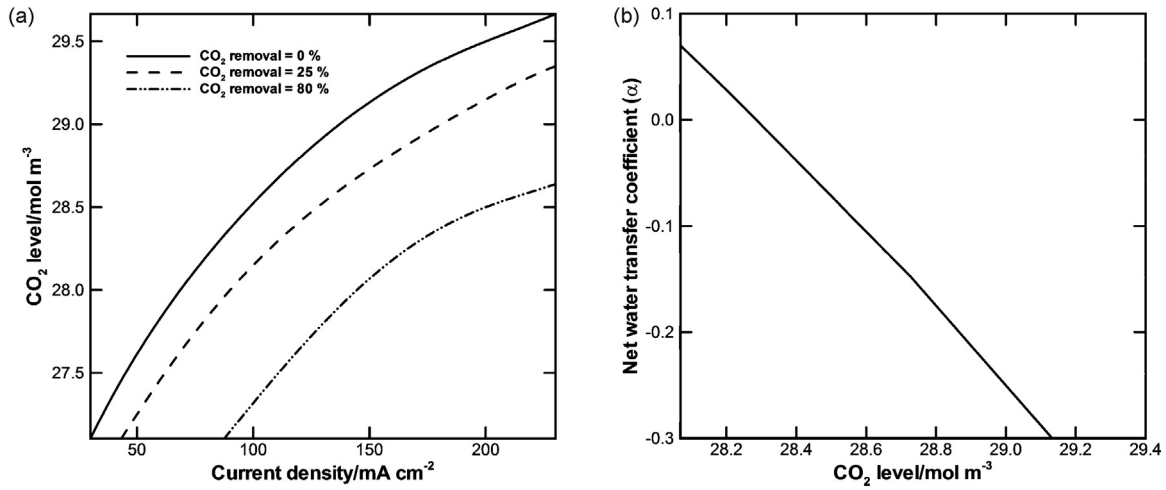

Fig. 10. (a) CO_2 level according to current density, (b) water transfer coefficient according to CO_2 level. (T_{cell} = 333 K, i = 150 mA cm^{-2}, ξ_a = 3.0, ξ_c = 3.0).

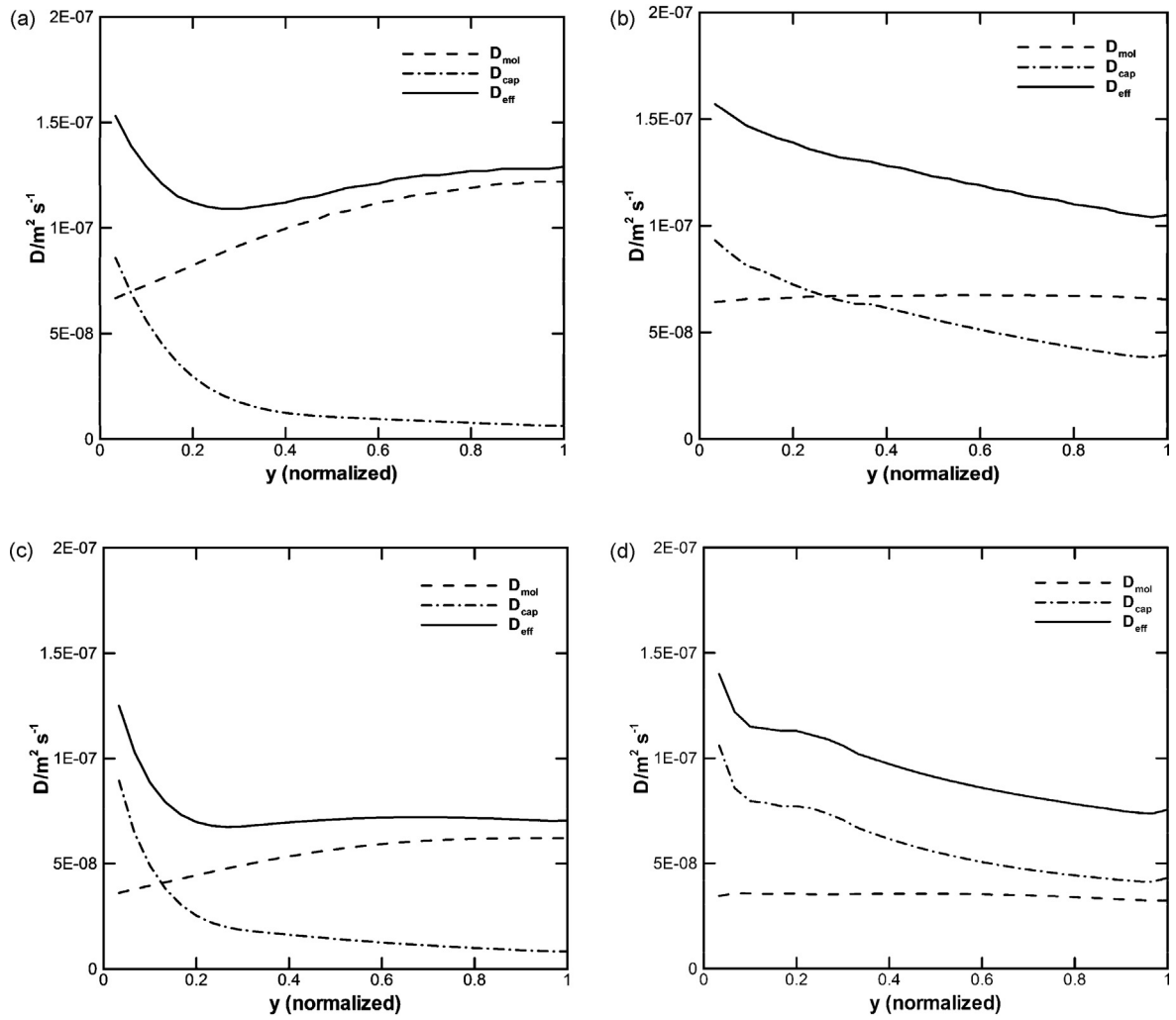

Fig. 11. Methanol diffusivity distribution in the anode channel direction: (a) Conventional DMFC (T_{cell} = 333 K, i = 150 mA cm^{-2}, ξ_a = 3.0, ξ_c = 3.0) (b) CO_2 breathing DMFC (T_{cell} = 333 K, i = 150 mA cm^{-2}, ξ_a = 3.0, ξ_c = 3.0) (c) Conventional DMFC (T_{cell} = 313 K, i = 150 mA cm^{-2}, ξ_a = 3.0, ξ_c = 3.0) (d) CO_2 breathing DMFC (T_{cell} = 313 K, i = 150 mA cm^{-2}, ξ_a = 3.0, ξ_c = 3.0).

is strong only at the inlet region and rapidly decreases since the anode becomes gaseous due to CO_2 accumulation (low liquid phase capillary diffusivity) and methanol concentration decreases in the channel direction by methanol consumption, i.e., methanol capillary factor decreases. As vapor/liquid molecular diffusivity of methanol becomes high at high temperature and two-phase molecular diffusivity of methanol is high under gaseous environment (see Fig. 3), two-phase molecular diffusivity of methanol increases in the channel direction and becomes the dominant mechanism of methanol transport. In the case of the CO_2

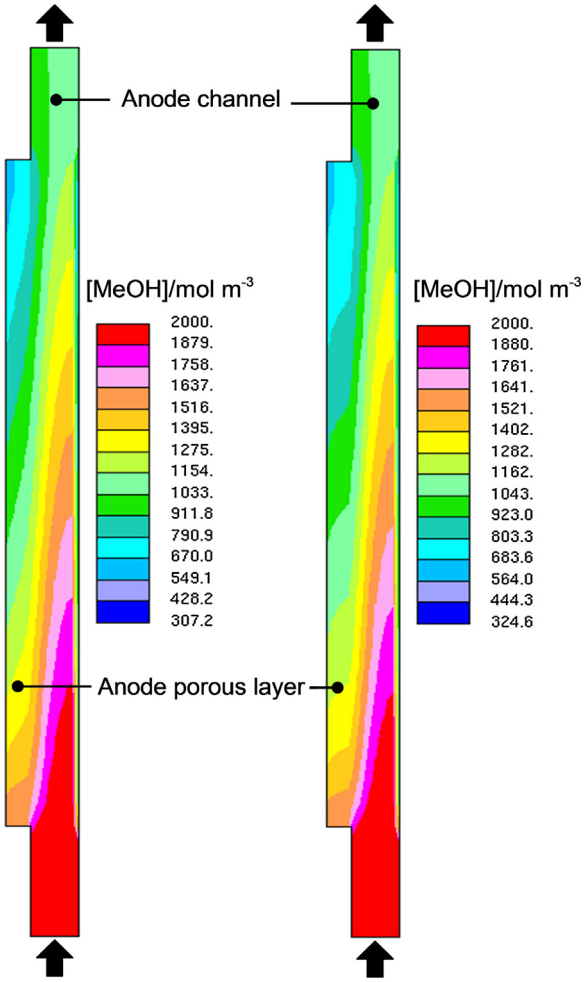

Fig. 12. Methanol concentration distribution (Section E), (left) conventional cell, (right) CO_2 breathing cell (T_{cell} = 333 K, i = 150 mA cm^{-2}, ξ_a = 3.0, ξ_c = 3.0).

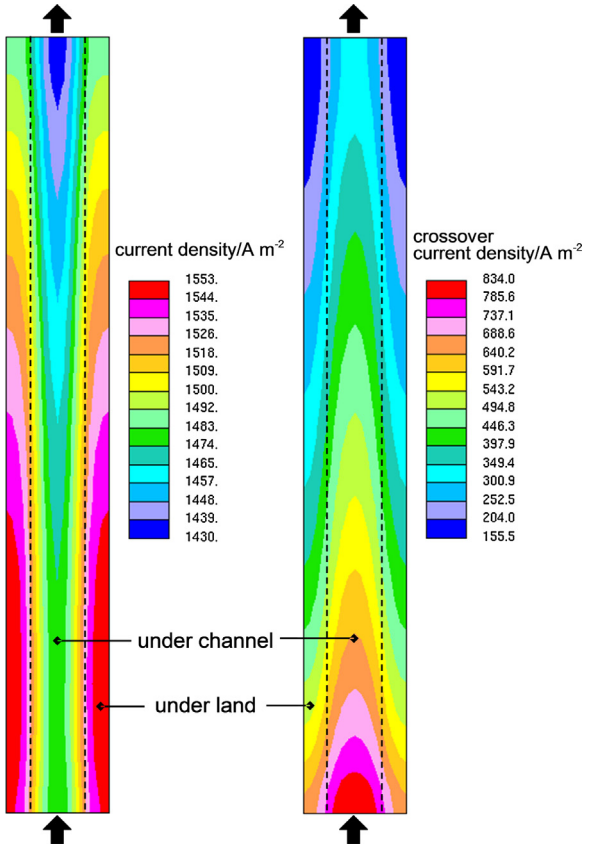

Fig. 13. (a) Local current density, (b) local crossover current density distribution in the conventional DMFC (T_{cell} = 333 K, i = 150 mA cm^{-2}, ξ_a = 3.0, ξ_c = 3.0).

breathing cell operating at high temperature (Fig. 11(b)), two-phase molecular diffusivity remains almost uniform in the channel direction due to CO_2 surface removal. Although liquid saturation level is uniform in the channel direction, methanol capillary diffusivity linearly decreases because methanol concentration decreases due to methanol consumption by MOR. When the cell temperature is low (T_{cell} = 313 K), methanol molecular diffusivity decreases but methanol capillary diffusivity increases. Overall effective diffusivity is slightly reduced compared to the high temperature case in the conventional cell (see Fig. 11(c)). Methanol capillary diffusion becomes dominant in the CO_2 breathing cell at low temperature as shown in Fig. 11(d). Methanol concentration distributions in the anode of both cells operating under the base condition are compared in Fig. 12. As both cells have similar effective methanol diffusivity, methanol concentration distributions are similar also.

CO_2 contributes to improving methanol molecular diffusion but prohibits methanol capillary diffusion. Although two-phase molecular diffusivity and capillary diffusivity of methanol are significantly affected by CO_2 level, effective methanol diffusivity which is the sum of both diffusivities, does not vary so much as shown in Fig. 11. This implies that anode performance of the CO_2 breathing DMFC should be not so different from that of conventional DMFCs. If there is no CO_2 in the anode porous media, there is no methanol capillary transport since liquid saturation is uniform everywhere and molecular diffusion occurs solely in liquid-phase, which is very low. Therefore, net methanol transport will be very poor. In that sense, maintaining some level of CO_2 inside the anode porous media is necessary for facilitating fuel transport. Even the CO_2 breathing DMFC, which has almost pure liquid flow in the anode channel, has a significant level of CO_2 inside the anode porous media, which enables the CO_2 breathing DMFC to have similar anode performance to the conventional DMFC.

3.4. Current density and methanol crossover

When the cathode condition is the same, methanol concentration distribution strongly affects current density and crossover current density distribution for both of the cells. As shown in Fig. 12, both cells have similar distribution of methanol concentration since they have similar effective methanol diffusivity. Current density and crossover current density distribution of the conventional cell operating under base condition are presented in Fig. 13(a) and 13(b). Since the CO_2 breathing cell shows similar result with the conventional cell, its figures are neglected here. Calculation results show that current density is high under the land region rather than under the channel region. This is because stoichiometry is large enough. Excessive amount of methanol, especially under the channel region, negatively acts by increasing methanol crossover, which leads to large anode overpotential and lower current density. As methanol concentration under the channel region is high, crossover current density is high there.

3.5. DMFC system efficiency

Cell voltage profiles are plotted according to operating temperatures in Fig. 14. The conventional cell and the CO_2 breathing cell didn't have significant difference each other. This result was anticipated from the overall effective methanol diffusivity discussed

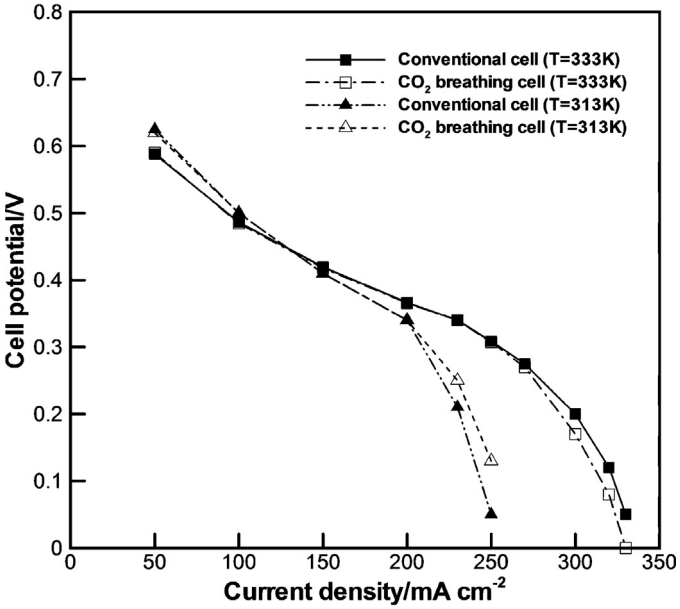

Fig. 14. Voltage profiles acquired from the simulation (2 M, $\xi_a = 3.0$, $\xi_c = 3.0$).

in the simulation section. In low current regime, lower temperature (313 K) is better for cell performance than higher temperature (333 K). When the cell operates at low current, methanol concentration near the anode catalyst layer becomes high since methanol consumption is low. This high methanol concentration leads to high methanol crossover. In addition, if the cell temperature is high, methanol diffusivity of the membrane becomes large. Therefore, crossover current density becomes large and cell voltage drops a bit.

The advantage of the CO_2 breathing DMFC does not come from the cell performance itself. As the required anode pressure of the CO_2 breathing DMFC is lower than that of the conventional cell, the mechanical efficiency is improved. The reversible thermodynamic efficiency of DMFC is defined as follows [26]:

$$\xi_{rev} = \frac{\Delta g}{\Delta h} = -\frac{nFE^0}{\Delta h} = 0.97 \quad (\text{at } 25^\circ\text{C}, 1 \quad \text{atm}) \tag{22}$$

However, actual voltage is much lower than this reversible voltage because of several voltage losses like ohmic loss, concentration loss and activation loss. Considering those voltage losses, the voltaic efficiency is expressed as follows:

$$\xi_{voltaic} = \frac{V_{cell}}{E^0} \tag{23}$$

In order to include fuel loss due to methanol crossover, fuel efficiency is defined as follows:

$$\xi_{fuel} = \frac{I}{I + I_{xover}} \tag{24}$$

Part of power generated by the cell is used for driving the system such as fuel pumping and air blowing. So we define the mechanical efficiency as follows:

$$\xi_{mech} = \frac{W_{elec} - W_a - W_c}{W_{elec}}$$

$$\text{where} \begin{cases} W_{elec} = I \cdot V \quad (\text{cell power output}) \\ W_a = \Delta p_a u_a A_a \quad (\text{fuel pumping power}) \\ W_c = \Delta p_c u_c A_c \quad (\text{air pumping power}) \end{cases} \tag{25}$$

Finally, the total energy efficiency of a DMFC can be expressed by

$$\xi = \xi_{rev}\xi_{voltaic}\xi_{fuel}\xi_{mech} \tag{26}$$

Fig. 15(a) shows the net power throughput according to the CO_2 removal amount. Although the cell polarization curve of the CO_2 breathing DMFC is similar to that of the conventional DMFC, cell performance is improved by saving pumping power required for fuel supply. Total energy efficiency according to CO_2 removal is presented in Fig. 15(b).

4. Experimental

Experiment was conducted to confirm the theoretical conclusion acquired from the simulation. Two different types of cells were prepared to compare the effect of CO_2 removal. One is the conventional DMFC and the other is the CO_2 breathing DMFC. Membrane-electrode assemblies (MEA) were fabricated using a combination of decal-transfer, direct-coating and hot-pressing methods. Commercial unsupported PtRu black (HiSPEC^{TM} 6000, Pt:Ru = 1:1 atomic ratio, Alfa Aesar) was used as anode catalyst, while commercial carbon-supported Pt (72.1 wt.% Pt on high surface area carbon, Tanaka, Kikinzoku Kogyo, K.K. Japan) was used as cathode catalyst. Catalysts (PtRu black or Pt/C) was mixed with di-ionized water, iso-propanol and ionomer solution (5 wt.% Nafion dispersion, 1100 EW, Dupont) using magnetic stirring and ultrasonication to form a catalyst ink. To obtain anode catalyst layers, the PtRu black catalyst ink was then coated onto the surface of decal (Teflon sheet) using spraying method with the aid of spraying gun (Iwata, Japan). The anode catalyst layer was transferred from the decal onto Nafion 212 membrane (Ion Power, Inc.) by hot-pressing at 398 K under 100 atm for 3 min. To obtain cathode catalyst layer, the Pt/C catalyst ink was coated directly onto another side of Nafion 212 membrane using spraying method. The PtRu and Pt catalyst loadings were ~8.5 and ~3.2 mg cm^{-2} in the anode and cathode catalyst layers, respectively. The contents of dry Nafion ionomer in the anode and cathode catalyst layers were ~27 wt.% and ~18 wt.%, respectively. 10wt% wet-proofed TGPH-90 carbon paper with micro-porous layer (MPL) and carbon cloth with MPL were used as anode and cathode diffusion media, respectively. To form a whole MEA, the anode and cathode diffusion media were hot-pressed together with the Nafion membrane with the anode and cathode catalyst layers at 398 K under 50 atm for 1.5 min. The active electrode area was 5 cm^2.

Fig. 16 shows the setup for the CO_2 breathing DMFC and the conventional DMFC. MEA were mounted between two identical Au-coated copper flow plates with single-path serpentine channels. The copper plates were also used as current collectors. For CO_2 breathing DMFC, a porous PTFE membrane with a thickness of 250 μm (M-R710 with a pore size of 0.8 μm and a porosity of 70%, FluoroTechniques Membrane Product, Inc.) was put between the anode copper plate and end plate with an open window in order to vent the CO_2 gas produced during DMFC operation from the anode flow channel into ambient atmosphere. When the open window was sealed with a plastic block, since CO_2 cannot be vented through porous PTFE membrane, the cell can be considered as a conventional DMFC. A digital pump (Series I digital pump, LabAllinace) with a range of 0.01-10 ml min^{-1} was used to deliver and control flow rate of aqueous methanol solution, while a digital mass flow controller (Omega Engineering, Inc) was used to measure and control flow rate of breathing-grade air. A digital temperature controller was used to control the electrical heater on the cell to maintain desired cell temperature. The cell temperature was set as 313 K.

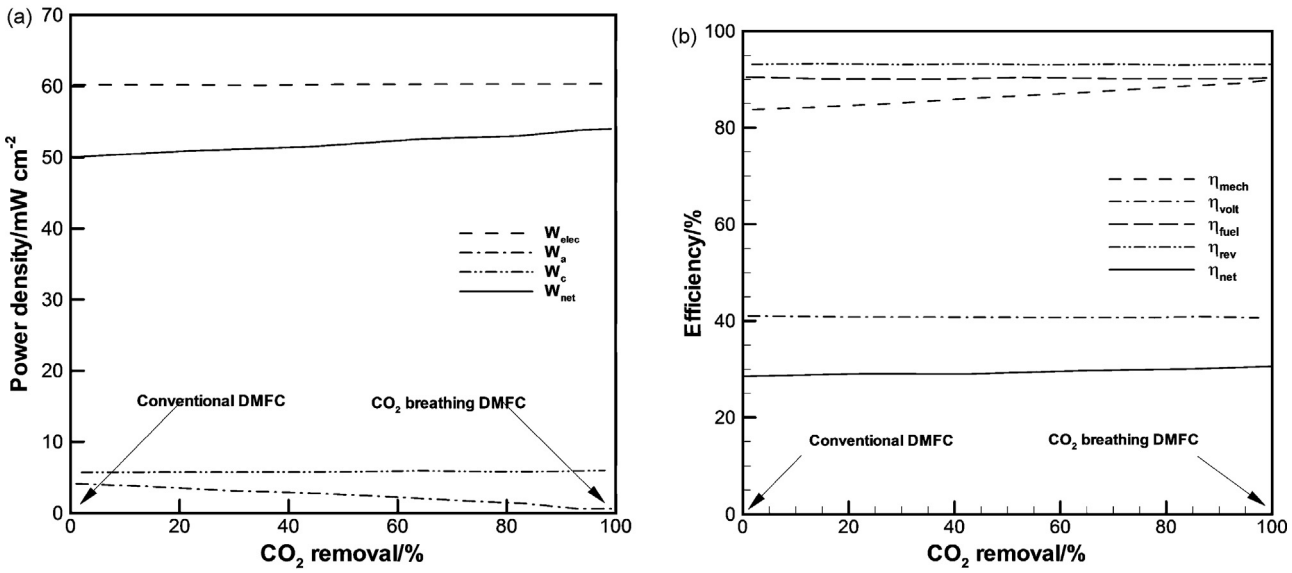

Fig. 15. Power throughput and system efficiency according to CO_2 removal.

For cell performance measurement, 2 M methanol solution was fed into the anode inlet at a flow rate of 0.12 ml min^{-1} (i.e. at a fuel stoichiometry of 3@150 mA cm^{-2}), while dry air with ambient pressure was fed into the cathode inlet at a flow rate of 67.9 ml min^{-1} (i.e. at an air stoichiometry of 5@150 mA cm^{-2}). Quick-scan cell performances were obtained by an Arbin testing system in a galvanodynamic mode with a scan rate of 10 mA s^{-1}, while the steady-state performances were obtained by an Arbin testing system in a galvanostatic mode with a current density of 150 mA cm^{-2}.

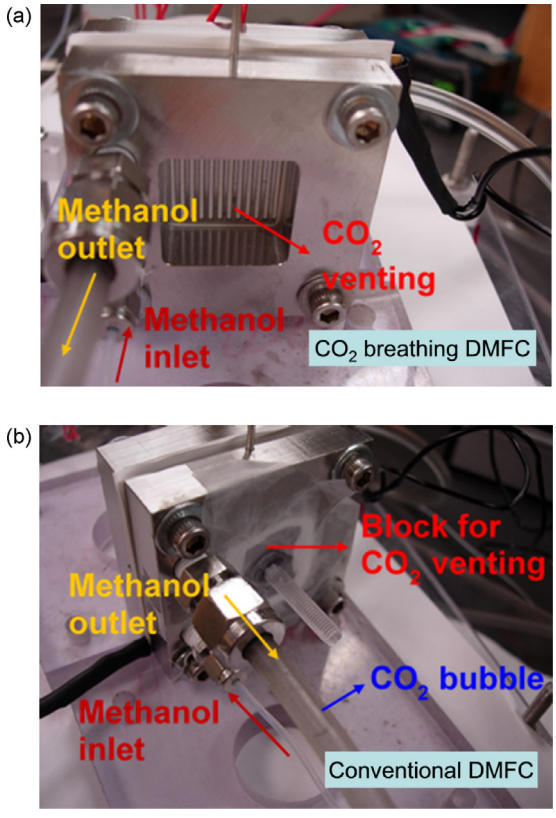

Fig. 16. Experimental setup for the present study: (a) CO_2 breathing DMFC (with CO_2 venting window is open), (b) Conventional DMFC (CO_2 venting window is blocked).

Anode polarization curves were obtained by an Arbin testing system in a galvanodynamic mode with a scan rate of 10 mA s^{-1}. Fully humidified hydrogen at a flow rate of 100 sccm was fed into the cathode, while 2 M methanol solution was fed into the anode at a flow rate of 0.12 ml min^{-1} (i.e. at a fuel stoichiometry of 3@150 mA cm^{-2}).

For the measurement of methanol crossover, dry N_2 at a flow rate of 100 sccm was fed into the cathode, while 2 M methanol solution was fed into the anode at a flow rate of 0.12 ml min^{-1} (i.e. at a fuel stoichiometry of 3@150 mA cm^{-2}). When a positive voltage was swept, the current obtained at N_2-fed cathode corresponded to the oxidation current of the total crossover methanol. The limiting current density was considered as the methanol crossover through the membrane from the anode to the cathode.

As shown in Fig. 16 (a), in the case of the CO_2 breathing DMFC, since the CO_2 produced from the methanol oxidation at the anode during the operation was vented through the porous PTFE membrane from the anode flow channels to ambient atmosphere, little gas bubble was observed in the tubing at the anode outlet. However, if the open window for CO_2 venting was blocked, as shown in Fig. 16 (b), CO_2 cannot be vented through the porous PTFE membrane, and then CO_2 had to be removed by methanol flow via two-phase flow in the anode flow channels. CO_2 gas bubbles can be observed continuously in the tubing at the anode outlet.

Fig. 17 (a) and Fig. 17 (b) show a comparison of quick-scan and steady-state cell performance between the CO_2 breathing DMFC and the conventional DMFC, respectively. With regard to quick-scan cell performance, a cell voltage of 0.409 V at 150 mA cm^{-2} was achieved at 313 K in the case of the CO_2 breathing DMFC, slightly lower than that in the case of the conventional DMFC. The peak power density of the CO_2 breathing DMFC was 72 mW cm^{-2}, which was ~8.3% lower than 78 mW cm^{-2} peak power density of the conventional DMFC. For 2 hour steady-state operation, when the cells were discharged at 150 mA cm^{-2} at 313 K, the CO_2 breathing DMFC achieved the same performance with an average cell voltage of 0. 416 V as the conventional one. When 2 M methanol was fed into the anode at a flow rate with a fuel stoichiometry of 3 at 150 mA cm^{-2}, the methanol crossover of the CO_2 breathing DMFC was 234 mA cm^{-2} at 313 K, slightly lower than that of the conventional one (i.e. 243 mA cm^{-2}), as shown in Fig. 17 (c). Anode overpotential according to current density of the CO_2 breathing DMFC was almost the same as that of the conventional one. For

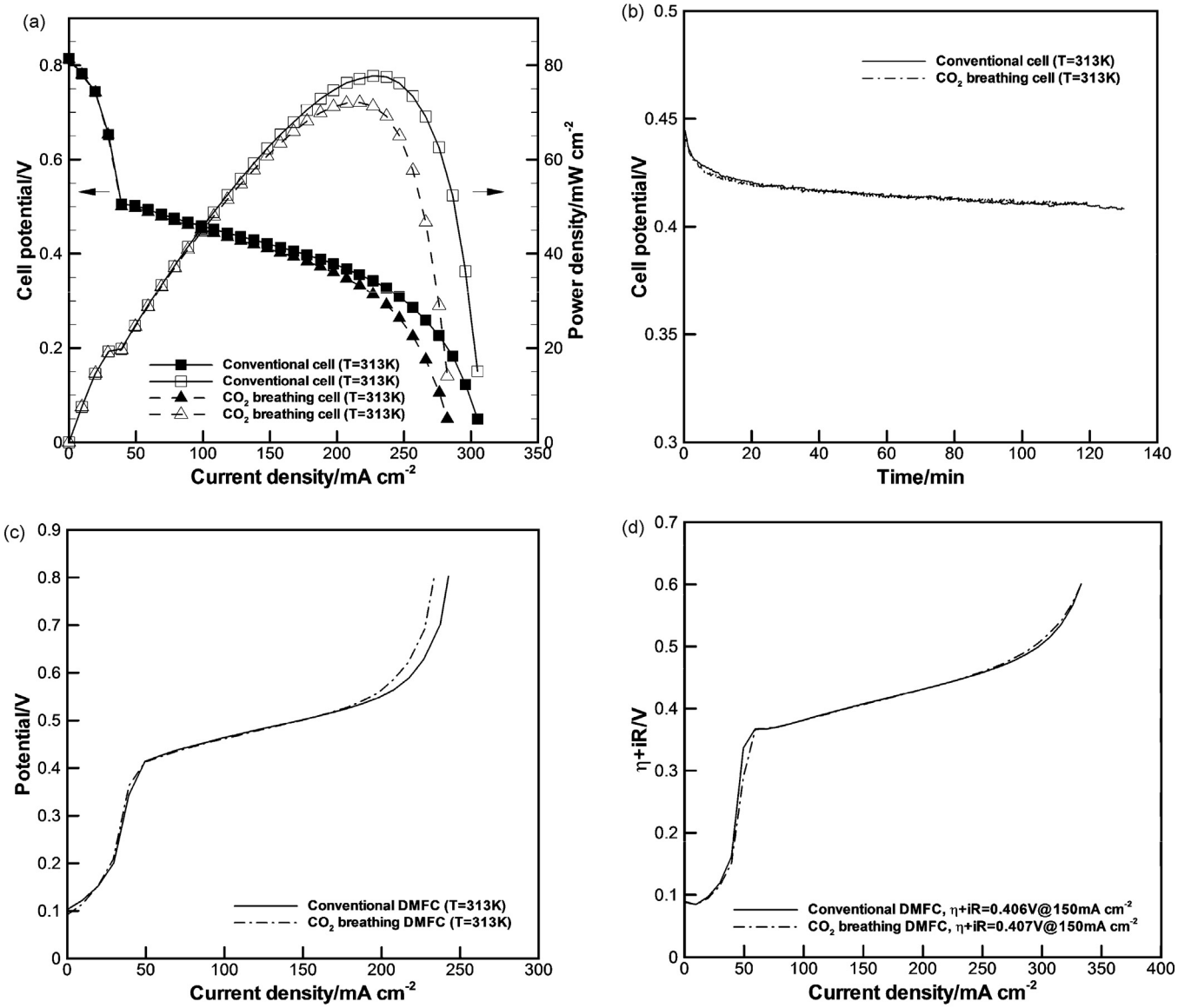

Fig. 17. Experiment result comparing the CO_2 breathing DMFC with the conventional DMFC (2 M, ξa = 3.0@150 mA cm^{-2}, ξc = 5.0@150 mA cm^{-2}, T_{cell} = 313 K): (a) Cell voltage and power density, (b) Steady-state cell voltage (i = 150 mA cm^{-2}), (c) Methanol crossover (ξa = 3.0@150 mA cm^{-2}), (d) Anode polarization curves (ξa = 3.0@150 mA cm^{-2}).

example, as shown in Fig. 17(d), at 313 K, the anode overpotential at 150 mA cm^{-2} was 0.406 and 0.407 V for the CO_2 breathing and the conventional DMFCs, respectively, which showed only 1 mV difference between both two cases. The negligible difference in the steady-state cell performance and anode overpotentials between two cases demonstrated that CO_2 can be vented through the porous membrane from the anode flow channels to the ambient atmosphere without scarifying any cell performance.

5. Conclusion

Fundamental analysis about two-phase water and methanol transport in a DMFC was conducted with multi-D DMFC model focusing on the role of CO_2 in mass transfer. As CO_2 level decreases, the net water transfer coefficient increases since CO_2 level controls capillary diffusivity and low CO_2 level builds wet condition in the anode, which drives much more water flux to the cathode side. The CO_2 breathing DMFC has uniformly wet anode porous media since CO_2 does not accumulate in the channel direction, which results in a larger water transfer coefficient than the conventional DMFC. Methanol transport in a DMFC is carried out by two-phase molecular diffusion and methanol capillary diffusion. It is found that CO_2 level controls molecular diffusion and capillary diffusion of methanol. When CO_2 level is high, two-phase molecular diffusion is enhanced while methanol capillary diffusion is suppressed. However, it is also found that CO_2 surface removal does not have as much effect on the methanol transport because the sum of molecular diffusivity and capillary diffusivity (the effective methanol diffusivity) is maintained at constant level. Therefore, the calculation result shows that the cell performances of the conventional cell and CO_2 breathing cell are not so much different each other. Improvement of the net energy efficiency came from the increased mechanical efficiency due to lowered anode pressure drop.

In order to confirm the theoretical finding, experiment was conducted to observe performance difference between the conventional and the CO_2 breathing DMFCs. As predicted from the simulation result, two cells didn't show significant performance difference each other although the cell dimension and the operating condition of the experiment were a bit different from that of the simulation case.

As the present model is a steady-state, volume-averaging model, it has limitation of capturing the dynamic phenomena such as bubble formation, coalescence and removal process. This bubble dynamics affects the cell performance especially under very low flow stoichiometry condition, which is rather obscure to express with a volume-averaging method using local liquid saturation. In the case of the CO_2 breathing DMFC, however, is free of being in trouble with bubbles since CO_2 bubbles emerged from the surface of GDL are immediately removed through the surface film. In the case of the conventional DMFC, a transient model which can capture the bubble dynamics should be developed in the future.

References

[1] P. Argyropoulos, K. Scott, W.M. Taama, Electrochemica Acta 44 (1999) 3575.
[2] G.Q. Lu, C.Y. Wang, J. Power Sources 134 (2004) 33.
[3] H. Yang, T.S. Zhao, Q. Ye, J. Power Sources 139 (2005) 79.
[4] H. Yang, T.S. Zhao, Electrochemica Acta 50 (2005) 3243.
[5] M.M. Mench, S. Boslet, S. Thynell, J. Scott and C.Y. Wang, Proceeding of the Symposium on Direct Methanol Fuel Cells, 199th Electrochemistry Society Proc. Series, Princeton, NJ, 2001.
[6] T. Bewer, T. Beckmann, H. Dohle, J. Mergel, D. Stolten, J. Power Sources 125 (2004) 1.
[7] Qiang Liao, Xun Zhu, Xueyan Zheng, Yudong Ding, J. Power Sources 171 (2007) 644.
[8] C.W. Wong, T.S. Zhao, Q. Ye, J.G. Liu, J. Electrochem. Soc., 152 A1600 (2005).
[9] K. Scott, P. Argyropoulos, P. Yiannopoulos, W.M. Taama, Journal of Applied Electrochemistry 31 (2001) 823.
[10] D. Michael, Lundin, J. Mark, McCready, J. Power Sources 172 (2007) 553.
[11] P. Argyropoulos, K. Scott, W.M. Taama, Chem. Eng. Journal 78 (2000) 29.
[12] A.A. Kulikovsky, Electrochemical communications 7 (2005) 237.
[13] A.A. Kulikovsky, Electrochemica Acta 51 (2006) 2003.
[14] J. Ge, H. Liu, J. Power Sources 163 (2007) 907.
[15] M.S. DeFilippis, MTI Mcirofuel Cells, Inc., U.S. Patent 7,081,310 B2 (2006).
[16] W.P. Acker, MTI Mcirofuel Cells, Inc., U.S. Patent 7,125,620 B2 (2006).
[17] D.D. Meng, C.J. Kim, J. Power Sources 194 (2009) 445.
[18] W. Liu, C.Y. Wang, J. Electrochem. Soc. 154 (2007), B352.
[19] S. Jung, J. Power Sources 231 (2013) 60.
[20] S. Jung, C.Y. Wang, J. Power Sources 248 (2014) 253.
[21] C.Y. Wang, P. Cheng, Int. Journal of Heat Mass Transfer 39 (1996) 3607.
[22] W. Liu, C.Y. Wang, J. Power Sources 164 (2007) 189.
[23] J.P. Meyers, J. Newman, J. Electrochem. Soc. (2002) 149, A710.
[24] J.P. Meyers, J. Newman, J. Electrochem. Soc. 149 (2002), A718.
[25] J.P. Meyers, J. Newman, J. Electrochem. Soc. 149 (2002), A729.
[26] E. Barendrecht, Fuel cell systems", 75, L.J.M.J. Blowen & M.N. Mugerwa, New York, 1993.
[27] R.H. Brooks, A.T. Corey, Hydrology Papers, 3, Colorado State University, 1964, pp. 1.
[28] R.B. Mrazek, C.E. Wicks, K.N.S. Prabhu, J. Chemical and Engineering Data 13 (1968) 508.
[29] B.E. Poling, J.M. Prausnitz, J.P. O'Connell, "The properties of Gases and Liquids", 5th ed., McGraw-Hill, New York, 2001.
[30] Z.J. Derlacki, A.J. Easteal, V.J. Edge, L.A. Woolf, Z. Roksandic, J. Physical Chemistry 89 (1985) 5318.
[31] T.A. Zawodzinski, C. Derouin, S. Radzinski, R.J. Sherman, V.T. Smith, T.E. Springer, S. Gottesfeld, J. Electrochem. Soc. 140 (1993) 1041.
[32] T.E. Springer, T.A. Zawodzinski, S. Gottesfeld, J. Electrochem. Soc. 138 (1991) 2334.
[33] G. Lu and, C.Y. Wang, an invited chapter for New Developments in Heat Transfer, Chapter 9, 317 (2005).
[34] T.A. Zawodzinski, J. Davey, J. Valerio, S. Gottesfeld, Electrochemica Acta 40 (1995) 297.